Journal of Materials Chemistry C

PAPER

View Article Online
View Journal | View Issue

Cite this: J. Mater. Chem. C, 2017, 5, 9761

A correlation between small-molecule dependent nanomorphology and device performance of organic light-emitting diodes with ternary blend emitting layers†

Francis Okello Odongo Ngome,[a] Young-Tae Kim,*[a] Hyeon-Dong Lee,[a] Young-Hoon Kim,[b] Tae-Woo Lee[bcd] and Chan-Gyung Park*[ae]

Received 1st June 2017,
Accepted 25th August 2017

DOI: 10.1039/c7tc02404e

rsc.li/materials-c

The morphology of emitting layers (EMLs) plays a vital role in determining the overall performance of solution processed phosphorescent organic light emitting diodes (PhOLEDs). Herein, the morphology of undoped small molecule binary blend EMLs prepared by blending tris(4-carbazoyle-9-ylphenyl)amine (TCTA) hole transport material (HTM) with a series of electron transport materials (ETMLs) was studied using a transmission electron microscope (TEM). Experimental results show that phase separation of the binary blend EMLs significantly depends on the polarity of the host. The binary blend ELMs were further doped with tris(2-phenylpyridine)-iridium(III) ($Ir(ppy)_3$) to form ternary blend EMLs and the resulting morphology was examined using scanning transmission electron microscopy-energy dispersive X-ray spectroscopy (STEM-EDS). The results report for the first time the existence of $Ir(ppy)_3$ needle-like aggregates in small molecule ternary blend EMLs. By comparing the size of the aggregates formed in small molecule ternary blend EMLs with those formed in polymer–small molecule blends, our results showed that small molecule blend EMLs exhibit minimal $Ir(ppy)_3$ aggregates with a low aspect ratio in contrast to polymer–small molecule blends. The effect of mixed solvent on the distribution of the aggregates was also examined using a TEM and an atomic force microscope (AFM). The disappearance of the aggregates with varying solvent mixture ratios signifies that solvent mixture is an effective way to control homogeneous distribution of $Ir(ppy)_3$ in the emitting layers of PhOLEDs. This was further evidenced by an improvement in light emitting efficiency and current efficiency of OLED devices fabricated using a mixed solvent.

1. Introduction

Organic light emitting diodes (OLEDs) have received a great deal of attention since their first introduction into the market in 1987 by C. W. Tang *et al.*[1] This is due to their superior properties such as high resolution from their self-emissive properties, flexibility, low power consumption, light weight, wide color gamut, wide viewing angle *etc.* which make them ideal for application in areas that require flat-panel displays and solid state lighting.[1–7] OLEDs are manufactured by thermal vacuum deposition and solution processing methods. The latter, however, is increasingly gaining much research interest due to its simplicity, low material waste, scalability and cost-effectiveness in large-area displays.[8–12] Nevertheless, one of the main issues in the solution processing technique is the ability to develop high performance-solution processed OLED materials.

To enhance the internal quantum efficiency (IQE) of OLEDs, significant efforts have been made towards broadening the exciton recombination zone to minimize the accumulation of charge density in the emitting layer which would otherwise result in triplet–triplet annihilation (TTA) as well as triplet–polaron annihilation (TPA).[13] This is achieved by employing a binary blend consisting of hole and electron transport materials to make emitting layers (EMLs).[5,14] By using a binary host, the chances of excitons recombining within the emitting layer can be boosted which leads to improved device performance. Furthermore, incorporation of phosphorescent dopants in the emitting layer has been adopted to upgrade the device efficiency. The phosphorescent guest materials can promote intersystem

[a] Department of Material Science and Engineering, Pohang University of Science and Technology (POSTECH), Pohang 790-784, South Korea. E-mail: yt1001@postech.ac.kr, cgpark1@postech.ac.kr
[b] Research Institute of Advanced Materials, Seoul National University, 1 Gwanak-ro, Gwanak-gu, Seoul 08826, Republic of Korea
[c] BK21PLUS SNU Materials Division for Education Creative Global Leaders, Seoul National University, 1 Gwana-ro, Gwanak-gu, Seoul 08826, Republic of Korea
[d] Department of Material Science and Engineering, Seoul National University, 1 Gwanak-ro, Gwanak-gu, Seoul 08826, Republic of Korea
[e] National Institute for Nanomaterials Technology (NINT), Pohang University of Science and Technology (POSTECH), Pohang 790-784, South Korea

† Electronic supplementary information (ESI) available. See DOI: 10.1039/c7tc02404e

crossing (IC) and increase the IQE to a theoretical maximum value of 100% by means of emissions from both singlet and triplet states.[16–20] Nonetheless, phosphorescent dyes at high concentration can sometimes cause deteriorated device performance through a quenching mechanism. For instance, J. J. Park *et al.* reported on the efficiency roll-off in solution processed small molecule PhOLEDs with highly doped ternary EMLs.[17] Additionally, degraded film morphology caused by phase separation/aggregation of the constituent hosts and guests is another serious factor that contributes to decreased IQE of OLEDs.[21–23] It is well known that the employed phosphorescent guest material such as tris(2-phenylpyridine)iridium(III) $Ir(ppy)_3$ tends to aggregate, especially when a high concentration is employed.[16] Furthermore, decreased luminescence lifetime in solution processed OLEDs caused by aggregation-induced self-quenching of dopant materials has been reported.[24–28] The morphological stability of EMLs and its impact on the device efficiency and lifetime can no longer be neglected.[29] Although homogeneous distribution of the Ir(ppy)3 dopant in the EMLs is crucial for enhanced device performance, in practice, this can be very hard to realize due to the influence of several other factors such as the dopant concentration, annealing temperature, and nature of the solvent employed. In addition, the use of non-doped self-host dendrimers which act as the host of the emissive cores themselves has been proposed as a potential approach of avoiding the tortuous doping technology as well as the inherent aggregation associated with the doping material in the EML. Nevertheless, not only are such materials limited, but also tuning their molecular structure could be quite convoluted.[13,30–32]

More recently, Y.-T. Kim *et al.* performed an *in situ* transmission electron microscope (TEM) experiment to elucidate the temperature dependent nanomorphology of Ir(ppy)3 doped polyvinyl carbazole (PVK:Ir(ppy)3) binary blend films.[26] In their findings, it was reported that the Ir(ppy)3 needle-like aggregates formed at high dopant concentration can be fine-tuned through optimization of annealing temperature to improve device performance. Although their work was based on polymer–small molecule blend EMLs, exploration of dopant distribution in the EMLs processed from purely small molecules is still limited. Small molecules exhibit several unique advantages such as well-defined chemical structure, high color purity, high charge mobility and efficiency which make them potential material candidates for solution processed OLEDs.[9,10,33,34] Nevertheless, to achieve better device operation, precise control of the morphology of small molecule based ternary blend emitting layers is still a great challenge owing to aggregation and phase separation of certain organic blends.[3,35]

Herein, we focus on the correlation between small-molecule dependent nanomorphology and device performance of PhOLEDs with ternary blend emitting layers. To investigate the effect of various electron transport materials on the EML morphology, the tris(4-carbazoyl-9-ylphenyl)amine (TCTA) hole transport material (HTL) was blended separately with 2-(4-*tert*-butylphenyl)-5-biphenylyl-1,3,4-oxadiazole (PBD), 4,4′-bis(carbazol-9-yl)biphenyl (CBP), 2,2′2″-(1,3,5-benzinetriyl)-tris(1-phenyl-1-*H*-benzimidazole) (TPBI) and tris(2,4,6-trimethyl-3-(pyridin-3-yl)-phenyl) borane (3TPYMB) electron transport materials (ETMs) to make binary blend films in a chlorobenzene solvent. The resulting morphologies of the films were investigated using conventional TEM. A similar procedure was repeated with the $Ir(ppy)_3$ incorporated in the mixture to form a ternary blend. A comparison between the Ir(ppy)3 dopant distribution in small molecule based EMLs with polymer based EML films was performed by substituting TCTA with PVK. Finally, a combinatorial approach to investigate the effect of different solvents on the film morphology and device performance was performed using a TEM and an atomic force microscope (AFM) on the TCTA:TPBI:Ir(ppy)3 based film. The experimental observations indicate that, the nature of solvent and host materials not only affects the film surface roughness but also film thickness and distribution of the Ir(ppy)3 dopant.

2. Experimental

The physical properties of the materials that were used here are presented in Table S1 (ESI†). All the employed host materials exhibit high triplet energy E_t with respect to the guest material which means that back flow of energy from the guest to host is inhibited. Additionally, TCTA was preferably selected for study due to its relatively high glass transition temperature (T_g) which guarantees device stability and also prevents temperature-induced crystallization during annealing.

Indium tin oxide (ITO)-patterned glass substrates were cleaned using acetone and 2-isopropanol (IPA) in an ultrasonification bath for 15 min, then boiled in IPA for 10 min. The cleaned substrates were UVO-treated for 15 min. Then, a GraHIL as a hole injection layer (HIL) was spin-coated and annealed at 150 °C for 15 min.[14,15,36] At the outset, small molecules of PBD, CBP, TPBI and 3TPYMB electron transport materials, each mixed with TCTA hole transport materials in the ratio 1 : 1, were dissolved in 0.4 wt% chlorobenzene (CB) solvent and then spin-coated on the PEDOT:PSS:PFI substrate. Then, the same procedure was repeated by incorporating 20 wt% of the $Ir(ppy)_3$ green phosphorescent dopant to make ternary blend emitting layers of TCTA:PBD:$Ir(ppy)_3$, TCTA:CBP:$Ir(ppy)_3$, TCTA:TPBI:$Ir(ppy)_3$, and TCTA:3TPYMB:$Ir(ppy)_3$. The dopant concentration of 20 wt% was chosen to clearly investigate the distribution of the $Ir(ppy)_3$ dopant and to show solvent-dependent morphological evolution of small molecule based ternary blend emitting layers. This is because such a high (20 wt%) dopant concentration can effectively induce the dopant aggregation.

For comparison, a separate experimental setup was used by substituting the TCTA hole transport material with a PVK polymer hole transport material to make PVK:3TPYMB:$Ir(ppy)_3$ and PVK:TPBI:$Ir(ppy)_3$ in chlorobenzene. It is important to note that the same (20 wt%) dopant concentration was used for both PVK and TCTA based ternary blend EMLs. Finally, to investigate the solvent-dependent $Ir(ppy)_3$ dopant distribution, TCTA:TPBI:$Ir(ppy)_3$ was prepared in a solvent mixture of (1) chlorobenzene (CB) and 1,2-dichlorobenzene (DCB), (2) CB and toluene in the ratios of 100 : 0, 75 : 25, 50 : 50, 25 : 75, 0 : 100 (wt%). The employed solvents exhibit varying physical properties such as boiling point, evaporation rate, polarity (as evidenced by varying dipole moments) and are commonly used as solvents in the

spin coating process (Table S2, ESI†). Besides, our main focus was based on how solvent polarity affects the distribution of TCTA:TPBI:Ir(ppy)$_3$ in the EMLs. The film samples for TEM observations were prepared by a floating technique which involves dissolving the HIL of PEDOT:PSS:PFI in distilled water leaving the EML comprising of TCTA:TPBI:Ir(ppy)$_3$ floating on the water surface which is then picked by the TEM mesh grid for analysis. This technique is employed prior to deposition of LiF electron injection layers (EILs) and Al cathodes. The morphological characterization of the blend films was performed using the TEM (JEM 2010F) set at an accelerating voltage of 200 kV. To characterize the distribution of iridium, energy dispersive X-ray spectrometry (EDS) of aberration-corrected scanning TEM (Cs-STEM) installed with a high angle annular dark field (HAADF) detector was employed.

For device fabrication, the ITO-patterned glass substrate with GraHIL was loaded into the N_2-filled glove box. Then, the TCTA : TPBI : Ir(ppy)$_3$ based emitting layer dissolved in varying solvent mixture ratios was deposited on the GraHIL containing ITO-patterned glass substrate at a speed of 500 rpm for 7 s and 3000 rpm for 90 s, followed by 20 min annealing at 40 °C. To deposit the electron transport layer (ETL) and the cathode, samples were loaded into the high vacuum chamber ($\sim 10^{-7}$ Torr). TPBI as an ETL, 1 nm-thick LiF and 100 nm thick Al cathode were subsequently thermally-deposited. The TEM cross-section of the complete device is shown in Fig. S1 (ESI†). The steady state photoluminescence (PL) spectra were recorded using a JASCO FP-8500 spectrofluorometer (excitation wavelength of 350 nm).

Topographical morphology characterization of the 40 °C annealed films were performed using VEECO Dimension 3100 AFM in a tapping mode with the following parameters: line scan of 512, scan size of 2.0 μm, scan rate of 0.996 Hz, aspect ratio of 1, integral gain of 0.2000, proportional gain of 0.8000 and tip velocity of 2000 Mv. The electrical properties of the thermally annealed samples were determined by their current density–voltage (J–V), current efficiency–voltage (I_{eff}–V), obtained using a source-meter (Keithley 236) while the luminance–voltage (L–V) characteristics were measured using a spectroradiometer (Minolta CS2000).

3. Results and discussion

The TEM bright field (BF) images of the small molecule binary blends of (a) TCTA:PBD, (b) TCTA:CBP, (c) TCTA:TPBI, and (d) TCTA:3TPYMB, which are spin-coated from chlorobenzene solvent (CB) are presented in Fig. 1. Both (a and b) exhibit heterogeneous morphology compared to (c and d) binary blend films, which suggest that TCTA exhibits good miscibility with TPBI and 3TPYMB under CB. The distinctive morphological variation of the blend films can be attributed to the chemical structure, dipole moment of the individual small molecules, and the type of solvent employed during spin-coating (Tables S1 and S2, ESI†). Since all the hosts employed were small organic molecules, the phase separation resulting from dissimilar

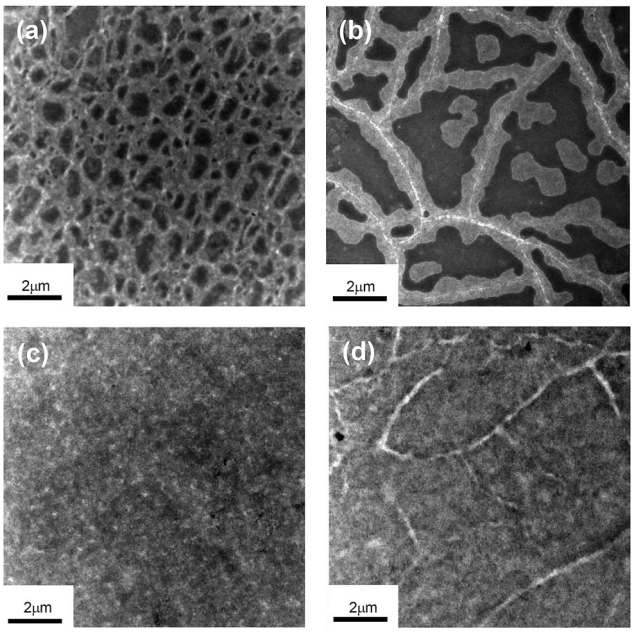

Fig. 1 TEM bright field morphologies of (a) TCTA:PBD, (b) TCTA:CBP, (c) TCTA:TPBI, and (d) TCTA:3TPYMB binary blend films spin-coated from chlorobenzene solvent.

molecular weights, which is commonly observed in polymer–small molecule blends may not occur in the present work.[27,37,38] Nonetheless, as shown in Fig. 1a and b, the polarity of the individual small molecules is likely to be the main factor contributing to phase separation in the film blends.[39] PBD is a weak polar material taking into account its structural geometry, whereas the chlorobenzene solvent and TCTA host material are polar. The dipole moments of biphenylyl and *tert*-butylphenyl side groups would cancel out and the nitrogen containing group would slightly contribute to the overall dipole moment. Furthermore, the non-polar benzene and the hydrophobic group of biphenylyl and *tert*-butylphenyl would prefer to segregate in a polar solvent resulting in phase separation (Fig. 1a). Conversely, the CBP molecule has a dipole moment of about 0.0 D which signifies non-polarity. Therefore, phase separation is likely to occur in a TCTA:CBP binary blend (Fig. 1b). On the other hand, TPBI and 3TPYMB both are polar materials as evidenced by their relatively high dipole moments of 3.0 D and 3.5 D respectively (Table S1, ESI†). Thus, a relatively more homogeneous film morphology is expected. Based on the experimental results, it can therefore be argued that the polarity of the individual small molecule blends played a key role in determining the final morphology of the emitting layers.

To improve the quantum efficiency of OLEDs, an Ir(ppy)$_3$ green dopant was incorporated into the previously studied blends to form ternary blend EMLs. The corresponding TEM images of (a) TCTA:PBD:Ir(ppy)$_3$, (b) TCTA:CBP:Ir(ppy)$_3$, (c) TCTA:TPBI:Ir(ppy)$_3$ and (d) TCTA:3TPYMB:Ir(ppy)$_3$ ternary blend films are shown in Fig. 2. Notably, the inhomogeneous morphology of PBD and CBP based ternary blend films still prevailed after incorporating green phosphorescent dye (insets of Fig. 2a and b). Such inhomogeneity is known to decrease the

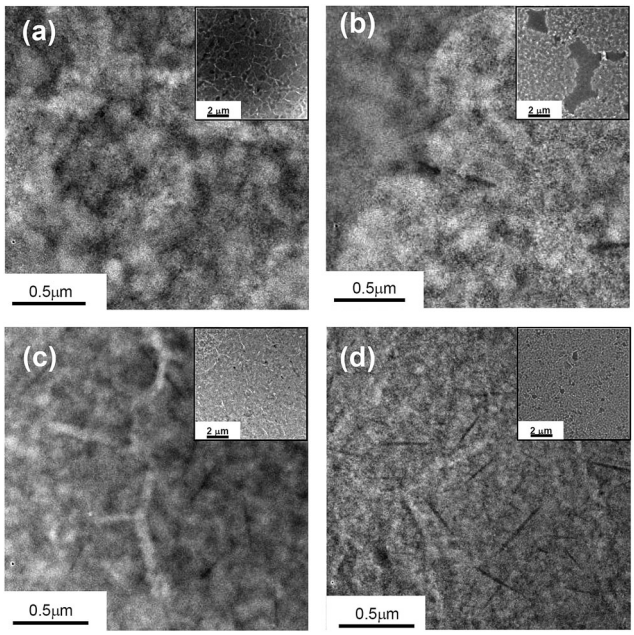

Fig. 2 TEM BF images of (a) TCTA:PBD:Ir(ppy)$_3$, (b) TCTA:CBP:Ir(ppy)$_3$ exhibiting phase separation (inset images), (c) TCTA:TPBI:Ir(ppy$_3$), and (d) TCTA:3TPYMB:Ir(ppy)$_3$ ternary blend films with needle-like aggregates.

device efficiency as it may account for current leakage and increased operational voltage.[40] Further analysis showed that the morphology of TCTA:TPBI:Ir(ppy)$_3$, TCTA:3TPYMB:Ir(ppy)$_3$ ternary blend emitting layers slightly became inhomogeneous after incorporating the Ir(ppy)$_3$ dopant. More intriguingly, the presence of needle-like aggregates with dark contrast, which was previously absent in the pre-doped binary blend films, corresponding to TCTA:TPBI (Fig. 1a) and TCTA:3TPYMB (Fig. 1b) were observed.

To elucidate the composition of the needle-like aggregates, we selected one of the samples (TCTA:TPBI:Ir(ppy)$_3$) containing the needle-like aggregates and performed additional tests using scanning TEM (STEM)-energy dispersive spectrometry (EDS). For the TEM analysis, the needle-like aggregates showed bright contrast in high angle annular dark field (HAADF) mode (Fig. S2b, ESI†). Based on common knowledge, the atomic number of an element determines its atomic scattering factor. Thus, heavy elements scatter more electrons and exhibit bright contrast in HAADF mode (Rutherford scattering cross-section is proportional to Z^2, where Z represents the atomic number). It is therefore convincing to argue that the needle-like aggregates represent Ir(ppy)$_3$ green dopant which contains iridium atoms of high atomic number.[41] This was further confirmed by the EDS mapping that showed green domains depicting iridium M_α signals corresponding to 1.977 eV (Fig. S2b, ESI†). The aggregation of the Ir(ppy)$_3$ dopant in the TCTA:TPBI:Ir(ppy)$_3$, TCTA:3TPYMB:Ir(ppy)$_3$ ternary blend films reveal poor miscibility between the dopant and the small molecule based host materials.

The formation process of the Ir(ppy)$_3$ needle-like aggregates has been explained in several ways. For instance, researchers have attributed the existence of the dopant aggregates as well as phase separation between the host and dopants to large interfacial energy difference. In other words, host–guest blends tend to form homogeneous film morphology, at decreased interfacial energy, while inhomogeneous morphology originating from phase separation of host–guest blends have been reported at increased interfacial energies.[21] To that end, we propose that the interfacial energy difference involved in the ternary blend films of TCTA:PBD:Ir(ppy)$_3$ and TCTA:CBP:Ir(ppy)$_3$ blends is likely to be large compared to that in TCTA:TPBI:Ir(ppy)$_3$ and TCTA:TPBI:Ir(ppy)$_3$ blends. In addition, the formation of the needle-like aggregates especially at high dopant concentrations has been expounded in terms of dipole–dipole interaction. In this study, the 20 wt% dopant concentration was employed. Therefore, increased dipole–dipole interaction is likely to cause self-assembly of the dopant molecules which subsequently leads to the formation of the Ir(ppy)$_3$ needle-like aggregates. This is because at high dopant concentration, the intermolecular distance is decreased and the dipole–dipole interaction of the high (6.26 D) dipole moment Ir(ppy)$_3$ small molecule is expected to increase. This is justified from the fact that dipole–dipole interaction between two molecules vary inversely as the third power of the distance between them.[42]

Another explanation for the formation of the needle-like aggregates is designated to offset π–π stacking between the neighboring aromatic rings in the chain of small molecules. With decreased distance between the neighboring aromatic rings, there exist electron–electron repulsion as well as electron–nucleus attraction between the benzene rings. This results in various molecular stacking geometries of which the most energetically stable π–π stacking is preferred.[22,38] Nevertheless, aggregation of the dopant material in the emitting layer not only increases the driving voltage due to inhomogeneous morphology but also decreases the light-emitting efficiency through bimolecular quenching.[20,21,43] This implies that meticulous control of the dopant distribution in the emitting layer of small molecule based OLEDs with ternary EMLs is inevitable.

Although several reports on surface morphology-dependent device performance are available, spectroscopic evidence elucidating the dopant aggregation-induced poor device performance, more particularly, in the solution processed small molecule based OLEDs is still limited. In this work, our novel report on the existence of Ir(ppy)$_3$ aggregates in the small molecule based solution processed OLEDs with ternary blend emitting layers has a great implication in attempting to unravel one of the root causes of luminance quenching in the solution processed small molecule OLEDs.

For comparison, polymer–small molecule ternary blend emitting layers of PVK:TPBI:Ir(ppy)$_3$, PVK:3TPYMB:Ir(ppy)$_3$ were also prepared and analyzed using conventional TEM (Fig. S3a and b, ESI†). The resulting morphologies were in contrast to those of TCTA:TPBI:Ir(ppy)$_3$ and TCTA:3TPYMB:Ir(ppy)$_3$ respectively (Fig. 2c and d). Our findings show that the Ir(ppy)$_3$ needle-like aggregations are less pronounced in the small molecule based emitting layers in contrast to the polymer–small molecule blend emitting layers. Although limited reports are available concerning the needle-like aggregation in polymer–small molecule binary blend EMLs of Ir(ppy)$_3$ doped

poly[9,9-di-*n*-hexyl-2,7-fluorene-*alt*-1,4-(2,5-di-*n*-hexyloxy)phenylene] (PFHP:$Ir(ppy)_3$), $Ir(ppy)_3$ doped PVK (PVK:$Ir(ppy)_3$), and $Ir(ppy)_3$ doped poly(3-hexylthiophene) (P3HT:$Ir(ppy)_3$), to the best of our knowledge, we for the first time, report the $Ir(ppy)_3$ needle-like aggregates in small molecule based ternary blend EMLs.[43–45] The average dimensions of the needle-like aggregates were 439 nm in length and 35 nm in width for the small molecule based ternary EMLs whereas an average length of 1053 nm and width of 70 nm were analyzed in the case of the polymer–small molecule based ternary emitting layers. In view of this, we can conclude that the aggregation of $Ir(ppy)_3$ is minimal in the small molecule based emitting layer as opposed to that of the polymer–small molecule based emitting layer. This is further supported by the fact that there is a small molecular weight difference in the small molecule based ternary blend emitting layers in contrast to the large molecular weight difference in the polymer–small molecule based ternary blend emitting layer. Therefore, it is reasonable to argue that by purely using small molecule host–guest blends during the spin-coating process, we are more likely to obtain EMLs with more homogenous morphology compared to polymer–small molecule blend systems.

Achieving EMLs with homogeneous morphology is a key factor to consider when designing high performance solution processed OLED devices. Phase separation of host blends and aggregation of dopants in the EMLs is detrimental to proper device performance. More particularly, host materials greatly influence device performance in terms of stability and lifetime.[22] This is because, phase separation between the host materials can generate increased host–guest distance *R*, where *R* represents the capture radius of guest molecules for efficient Foster energy transfer process.[46] In this study, we selected the TCTA:TPBI:$Ir(ppy)_3$ based EML with relatively homogeneous morphology out of the four prepared sets of small molecule based ternary EMLs and focused on controlling the distribution of the $Ir(ppy)_3$ dopant through the solvent mixture method. The solvent method was adopted because of its simplicity and due to the fact that most of the commonly used solvents are already available on the market. Moreover, many researchers have also proposed the method as an effective way of dissolving certain organic molecule blends with poor miscibility.[47] For instance, M. H. Rezvani *et al.* employed aromatic and non-aromatic solvents with different evaporation rates to tune the electrical properties of polymer–small molecule PhOLEDs comprising PVK:PBD:C6(3-(2-benzothiazolyl)-7-(diethylamino) coumarin) emitting layers.[30] Nevertheless, they failed to present in their work spectroscopic evidence correlating the emitting layer morphology and the device performance.

In our work, we provide direct evidence on solvent dependent $Ir(ppy)_3$ dopant distribution as well as the overall morphological evolution of the EML and its impact on the device performance. The TEM analysis was conducted on the TCTA : TPBI : $Ir(ppy)_3$ ternary blend EMLs spin-coated from the solvent mixtures of varying ratios. Fig. 3a–e represents the TEM BF images of the TCTA : TPBI : $Ir(ppy)_3$ based emitting layers spin-coated from DCB and CB solvent blends, while Fig. 3f–j shows the same emitting layer structure spin-coated from a CB : toluene solvent blend with different blending ratios. Based on the results, it is evident that the $Ir(ppy)_3$ needle-like aggregates initially present in the TCTA : TPBI : $Ir(ppy)_3$ ternary blend prepared from chlorobenzene disappear with increasing dichlorobenzene (DCB) ratio (Fig. 3a–d). DCB solvent exhibits a high dipole moment of 2.27 D which is higher than that of CB. This implies that DCB is more polar compared to CB (Table S2, ESI†). We can therefore expect enhanced dissolution of the $Ir(ppy)_3$ dopant with less or no aggregates formed when DCB is used. However, it is worth mentioning that the thickness of the EML fabricated from 100% DCB is too thin for normal operation of the device and therefore, the thickness is controlled by blending DCB with CB. We also observed that the needle-like aggregates completely disappear at 50 wt% DCB mixed with 50 wt% CB (expressed as 50DCB : 50CB) as shown by the TEM image in Fig. 3c. Surprisingly, although toluene is a non-polar solvent, the needle-like aggregates also disappeared with increasing toluene ratio (Fig. 3g–j). This is quiet inconsistent with some of the previous research findings which proposed the use of a high polar solvent to enhance dispersion of the highly polar $Ir(ppy)_3$ dopant during spin-coating.[24,40] Even though, we cannot accurately explain the dynamics behind dissolution of the $Ir(ppy)_3$ in toluene solvent, we speculate that other than polarity of the solvent employed, other factors such as dipole-induced dipole and dispersion

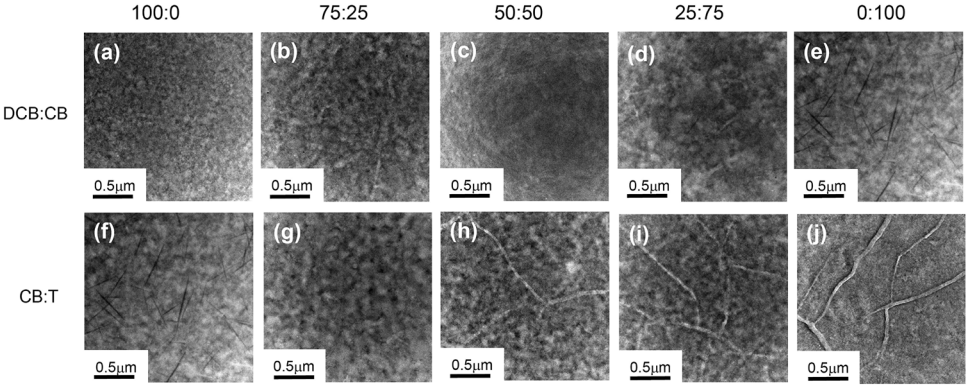

Fig. 3 TEM BF images of solvent effect nanomorphology of TCTA : TPBI : $Ir(ppy)_3$ based devices spin-coated from (a–e) DCB : CB and (f–j), CB : toluene solvent. The mixing ratios are in terms of wt%.

forces might as well contribute to the dissolution of the $Ir(ppy)_3$ aggregates.[48]

To further interrogate the evolution of the needle-like aggregates with increasing toluene solvent, steady-state photoluminescence (SSPL) measurements were performed. As can be observed in Fig. S4 (ESI†), the hypsochromic shift of the SSPL from 520 nm to 510 nm (low to high wavelength) further signals the disappearance of the needle-like aggregates which is consistent with our TEM findings (Fig. 3). Furthermore, it is well documented that a decrease in the molecular aggregate due to low conjugation is accompanied by a hypsochromic shift in the SSPL.[56] Nevertheless, as would be expected, the emitting layer morphology of the toluene based films deteriorated with increasing toluene ratio (Fig. 3j). The deteriorated film morphology can be attributed to the high evaporation rate constant of toluene which is 6.1, Table S2 (ESI†). This implies that fast depletion of toluene solvent molecules would lead to a decreased solvent–solute interaction time, which is the prerequisite for poor thinning and inhomogeneous spread of the film.[49]

The electrical properties *i.e.*, (a) current density, (b) luminance–voltage, (c) current efficiency and (d) electroluminescence intensity–wavelength characteristics of the solution processed small molecule PhOLED devices fabricated from different solvent blends are presented in Fig. 4. A summary of the electrical properties of all the devices is also shown in Table 1. Other than the electroluminescence intensity, other device electrical characteristics varied significantly depending on the type of solvent employed. From the current density–voltage characteristics (Fig. 4a), the high current density value observed in the device prepared from DCB can be assigned to the reduced EML thickness. The effective electric field depends on the EML thickness, *i.e.* thinner layers experience higher electric field at a given voltage corresponding to higher current density.[30,53] On the other hand, devices prepared from toluene solvent exhibited lower current density which is due to thick inhomogeneous EMLs.

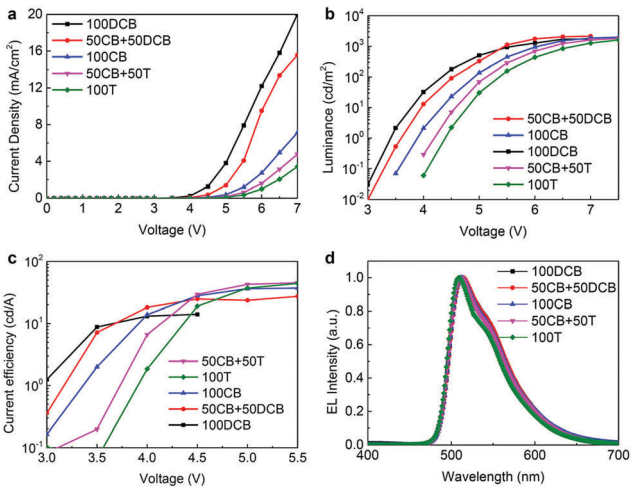

Fig. 4 (a) Current density–voltage, (b) luminance–voltage, (c) current efficiency–voltage, and (d) electroluminescence–wavelength characteristics of TCTA:TPBI:$Ir(ppy)_3$ devices spin-coated from varying solvent blends.

Table 1 Summary of solvent-dependence device electrical performance

Solvent ratio (wt%)	Operating voltage (V_t)	Max. luminance (cd m^{-2})	Max. current density (mA cm^{-2})	Max. current efficiency (cd A^{-1})
100DCB	3.5	1725.3	20.1	14.1
50DCB : 50CB	3.5	2116.5	16.2	27.3
100CB	4.0	1967.1	9.68	37.1
50CB : 50T	4.5	1869.0	7.1	45.3
100T	5.0	1599.3	5.8	44.1

The luminance–voltage characteristics (Fig. 4b) indicate that the device prepared from 50DCB : 50CB exhibited the highest luminance of 2116.5 cd m^{-2}. This is in agreement with the TEM observation in Fig. 3c, which shows the absence of the $Ir(ppy)_3$ needle-like aggregates. This improved luminance performance can be attributed to the enhanced dopant dispersion within the EML as a result of blending the CB solvent with a high dipole moment DCB solvent. Controlling the $Ir(ppy)_3$ dopant distribution in the EML is crucial for enhancing emissions from both singlet and triplet excitons as well as decreasing bimolecular quenching.[20,21,25]

On the other hand, the device prepared from 50 wt% CB mixed with 50 wt% toluene (expressed as 50CB : 50T) showed the highest current efficiency of 45.17 cd A^{-1} (Fig. 4c). The relatively lower current efficiency of our solution-processed OLEDs compared to the ones in the previous literature is possibly due to the high dopant concentration of 20 wt% which was chosen to induce the aggregation in the emitting layer.[36]

To investigate other possible cause for this, we examined the TEM cross-sections of the devices (Fig. 5). It is well known that the EML thickness plays an important role in determining the performance of OLEDs.[30,50–52] Although our results could not define the exact EML thickness due to low contrast of organic layers comprising TPBI, EML, PEDOT:PSS:PFI, we could clearly notice the increment in the thickness of the organic layer regions with change in solvent from CB to toluene. It is worth noting that the thickness of TPBI and PEDOT:PSS:PFI for all the devices as measured by ellipsometry were constant due to identical processing conditions. Based on our results, we suggest that the origin of the enhanced current efficiency observed in the 50CB : 50T based EML was due to thicker EML thickness with relatively homogeneous surface morphology.[30,53,54] The thicker EML signifies a broader electron–hole recombination zone which consequently results in the improved current efficiency. On the other hand, although the device prepared from 100% toluene solvent exhibited the thickest emitting layer, its morphology was severely deteriorated (Fig. 5d). We therefore argue that the inhomogeneous morphology resulted in poor contact between the organic layers and the electrodes leading to the low luminance, as well as high operating voltage recorded.[48–55]

Furthermore, the interface between the electrodes and the organic layers is known to play a crucial role in determining the efficiency of charge carrier injection from the electrodes to the active emitting layer.[44,45] The large difference in the vapor pressure as well as the evaporation rate constant of the employed solvents greatly affected the thickness of the emitting

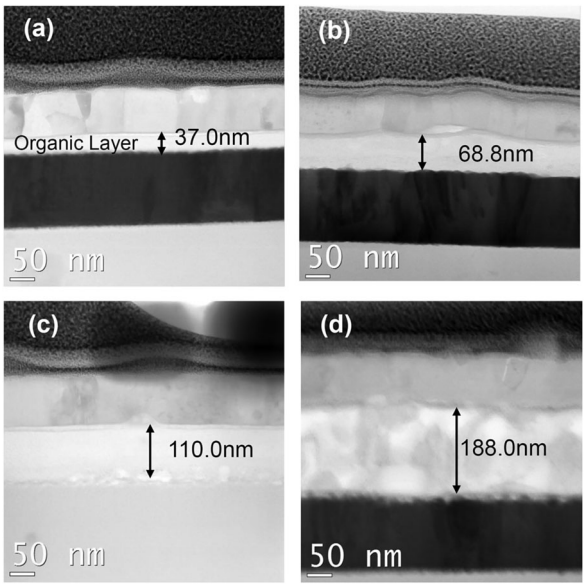

Fig. 5 STEM BF cross-sections of TCTA:TPBI:Ir(ppy)$_3$ based small molecule devices fabricated from (a) 50DCB : 50CB, (b) CB, (c) 50CB : 50toluene and (d) 100% toluene. Notably, EML spin-coated from 100% DCB was too thin to be prepared by the FIB technique hence it was not included here.

layer, *i.e.* toluene solvent, is characterized by high vapor pressure and high evaporation rate constants of 20 hPa and 6.1 respectively (Table S2, ESI†). Therefore, toluene based films would be expected to freeze faster and concurrently lead to an increase in the layer thickness.[49] The reverse behavior was observed in chlorobenzene and dichlorobenzene solvent respectively. Blending the solvents significantly tunes the EMLs. However, it is worth noting that, the imperfect optimization of experimental conditions still contributed to the large change in the EML thickness with solvent variation.

Fig. 4d indicates electroluminescent peaks at around 514 nm which well matched with EL peaks in the green emitting Ir(ppy)$_3$ dopant in all the devices. These sharp peaks suggest that sufficient energy transfer occurred from the host to guest materials in all the devices. Although it is known that the EML film thickness affects the device properties, the present work attempts to elucidate the nanomorphology dependent device performance of organic light emitting diodes with ternary blend emitting layers. More importantly, we employed solvent mixture to aim at expounding on the distribution of Ir(ppy)$_3$ within the EML as well as the overall morphology of the EML depending on the type of solvent used.

AFM analysis was performed to further explore solvent dependent-surface morphology and device performance. The root mean square roughness (RMS) of the EMLs fabricated from 50DCB : 50CB, CB, 50CB : 50T, toluene is presented in Fig. 6. Based on the results, it is evident that the film surface roughness increases from 0.2 nm of 50DCB : 50CB to 0.7 nm of toluene. This is in agreement with our previous TEM results shown in Fig. 3 (inset images). For further clarification, we considered the evaporation rates of DCB, CB and toluene solvents presented in Table S2 (ESI†).[57,58] Toluene, which has the highest evaporation rate constant of 6.1, is expected to vaporize much faster during spin-coating. This implies that not enough time is available for solvent–solute interaction consequently resulting in the inhomogeneous film morphology observed. By blending toluene with chlorobenzene, the high

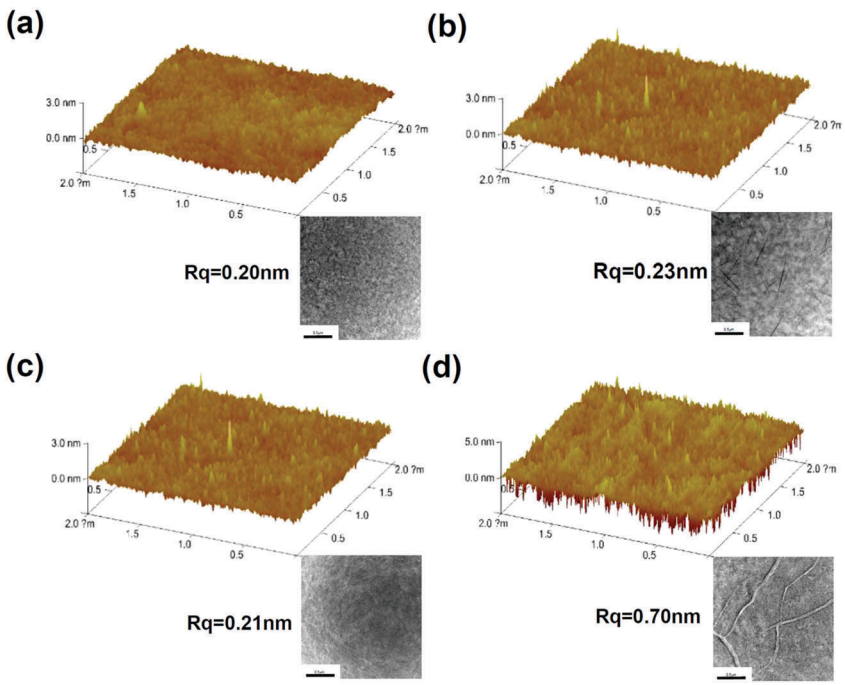

Fig. 6 AFM images of EMLs prepared from (a) 50DCB : 50CB, (b) CB, (c) 50DCB : toluene, and (d) toluene solvent, respectively. The corresponding TEM images are shown on the right side of each AFM image.

evaporation rate of toluene solvent is fine-tuned accordingly thereby improving the EML morphology and subsequently the device performance.

Although the device processing conditions were not perfectly optimized for all the devices, nevertheless, our main objective of presenting a direct evidence on the distribution of the $Ir(ppy)_3$ dopant as well as solvent-dependent morphological evolution of small molecule based ternary blend EMLs was successfully achieved. The devices consisting of the emitting layers made from 50DCB : 50CB and 50CB : 50T showed enhanced luminance and current efficiency, respectively, which is attributed to the improved dopant distribution and relatively homogeneous film morphology. However, further advancement can be made by controlling other processing parameters such as spin-coating speed and annealing temperatures to achieve high performance small molecule based optoelectronic devices.

4. Conclusions

The effects of host materials, solvent type and dopant distribution on the morphology of solution processed small molecule based ternary blend emitting layers were investigated. The main findings can be summarized as follows:

(1) The polarity of host materials significantly influences the emitting layer morphology *i.e.* host materials of comparable polarity are more likely to form homogeneous emitting layers.

(2) For the first time, a STEM-EDS study on the $Ir(ppy)_3$ dopant distribution in the small-molecule based ternary blend emitting layer revealed the existence of $Ir(ppy)_3$ dopant needle-like aggregates. This is also confirmed by variation in the peak shift as illustrated by the steady state photoluminescence spectra.

(3) The size of the $Ir(ppy)_3$ needle-like aggregates are less pronounced in small molecule ternary blend emitting layers (TCTA:TPBI:$Ir(ppy)_3$) compared to polymer–small molecule ternary blend emitting layers (PVK:TPBI:$Ir(ppy)_3$).

(4) Mixed solvent can be employed to fine-tune the distribution of the $Ir(ppy)_3$ dopant material as well as to improve the overall morphology of solution processed small molecule based films.

We believe that our experimental approach has a great potential for application not only in solution processed small molecule based OLED devices but also in polymer–small molecule blend films.

Conflicts of interest

There are no conflicts of interest to declare.

Acknowledgements

The authors gratefully acknowledge the generous financial support of the National Institute for Nanomaterials Technology (NINT) in POSTECH.

References

1 B. Wang, L. Zhang, Y. Hu, X.-B. Shi, Z.-K. Wang and L.-S. Liao, *J. Mater. Chem. C*, 2016, **4**, 6570–6574.
2 Z. Zhao, J. W. Lam and B. Z. Tang, *J. Mater. Chem.*, 2012, **22**, 23726–23740.
3 L. Duan, L. Hou, T.-W. Lee, J. Qiao, D. Zhang, G. Dong, L. Wang and Y. Qiu, *J. Mater. Chem.*, 2010, **20**, 6392–6407.
4 M. Mas-Torrent and C. Rovira, *Chem. Soc. Rev.*, 2008, **37**, 827–838.
5 A. Hayer, R. Anémian, T. Eberle, S. Heun, A. Ludemann, N. Schulte and H. Buchholz, *J. Inf. Disp.*, 2011, **12**, 57–59.
6 K. Goushi, K. Yoshida, K. Sato and C. Adachi, *Nat. Photonics*, 2012, **6**, 253–258.
7 N. Deshapande, N. S. Belavagi, M. G. Sunagar, S. Gaonkar, G. Pujar, M. Wari, S. Inamdar and I. A. M. Khazi, *RSC Adv.*, 2015, **5**, 86685–86696.
8 J. Chen, C. Shi, Q. Fu, F. Zhao, Y. Hu, Y. Feng and D. Ma, *J. Mater. Chem.*, 2012, **22**, 5164–5170.
9 S. R. Forrest, *Nature*, 2004, **428**, 911–918.
10 N. J. Findlay, B. Breig, C. Forbes, A. R. Inigo, A. L. Kanibolotsky and P. J. Skabara, *J. Mater. Chem. C*, 2016, **4**, 3774–3780.
11 K. S. Yook and J. Y. Lee, *Adv. Mater.*, 2014, **26**, 4218–4233.
12 S. Kappaun, C. Slugovc and E. J. List, *Int. J. Mol. Sci.*, 2008, **9**, 1527–1547.
13 Y. Wang, Y. Lu, B. Gao, S. Wang, J. Ding, L. Wang, X. Jing and F. Wang, *Chem. Commun.*, 2016, **52**, 11508–11511.
14 Y. R. Cho, H. S. Kim, Y.-J. Yu and M. C. Suh, *Sci. Rep.*, 2015, 5.
15 T.-H. Han, Y.-H. Kim, M. H. Kim, W. Song and T.-W. Lee, *ACS Appl. Mater. Interfaces*, 2016, **8**, 6152–6163.
16 M. A. Baldo, D. O'brien, Y. You, A. Shoustikov, S. Sibley, M. Thompson and S. Forrest, *Nature*, 1998, **395**, 151–154.
17 J. J. Park, S. T. Lee, T. J. Park, W. S. Jeon, J. Jang, J. H. Kwon and R. Pode, *J. Korean Phys. Soc.*, 2009, **55**, 327–330.
18 Y. Tao, Q. Wang, C. Yang, K. Zhang, Q. Wang, T. Zou, J. Qin and D. Ma, *J. Mater. Chem.*, 2008, **18**, 4091–4096.
19 C. Yao, Q. Cui, J. Peng, X. Xu, R. Liu, J. Wang, Y. Tian and L. Li, *J. Mater. Chem. C*, 2015, **3**, 5017–5025.
20 S. Reineke and M. A. Baldo, *Phys. Status Solidi A*, 2012, **209**, 2341–2353.
21 L. Liu, B. Zhang, Z. Xie, J. Ding and L. Wang, *Org. Electron.*, 2013, **14**, 55–61.
22 Y. Zhang and H. Aziz, *ACS Appl. Mater. Interfaces*, 2016, **8**, 14088–14095.
23 C. Fan, Y. Lei, Z. Liu, R. Wang, Y. Lei, G. Li, Z. Xiong and X. Yang, *ACS Appl. Mater. Interfaces*, 2015, **7**, 20769–20778.
24 S. Takayasu, T. Suzuki and K. Shinozaki, *J. Phys. Chem. B*, 2013, **117**, 9449–9456.
25 Z. Gao, F. Wang, K. Guo, H. Wang, B. Wei and B. Xu, *Opt. Laser Technol.*, 2014, **56**, 20–24.
26 Y. T. Kim, Y. H. Kim, J. B. Seol, T. W. Lee and C. G. Park, *Phys. Chem. Chem. Phys.*, 2015, **17**, 21555–21563.
27 K. Zhao, O. Wodo, D. Ren, H. U. Khan, M. R. Niazi, H. Hu, M. Abdelsamie, R. Li, E. Li and L. Yu, *Adv. Funct. Mater.*, 2016, 1737–1746.

28 L. Liu, X. Liu, B. Zhang, J. Ding, Z. Xie and L. Wang, *J. Mater. Chem. C*, 2015, **3**, 5050–5055.
29 A. R. Smith, J. L. Ruggles, H. Cavaye, P. E. Shaw, T. A. Darwish, M. James, I. R. Gentle and P. L. Burn, *Adv. Funct. Mater.*, 2011, **21**, 2225–2231.
30 M. H. Rezvani, F. Farajollahi, A. Nikfarjam, P. Bakhtiarpour and E. Saydanzad, *Materials*, 2013, **6**, 1994–2006.
31 S. Wang, B. Zhang, Y. Wang, J. Ding, Z. Xie and L. Wang, *Chem. Commun.*, 2017, **53**, 5128–5131.
32 Y. Wang, S. Wang, J. Ding, L. Wang, X. Jing and F. Wang, *Chem. Commun.*, 2017, **53**, 180–183.
33 M. Y. Lo, C. Zhen, M. Lauters, G. E. Jabbour and A. Sellinger, *J. Am. Chem. Soc.*, 2007, **129**, 5808–5809.
34 E. S. Hellerich, J. J. Intemann, M. Cai, R. Liu, M. D. Ewan, B. C. Tlach, M. Jeffries-EL, R. Shinar and J. Shinar, *J. Mater. Chem. C*, 2013, **1**, 5191–5199.
35 S. Ho, S. Liu, Y. Chen and F. So, *PHOTOE*, 2015, **5**, 057611.
36 T.-H. Han, M.-R. Choi, C.-W. Jeon, Y.-H. Kim, S.-K. Kwon and T.-W. Lee, *Sci. Adv.*, 2016, **2**, e1601428.
37 T. Ohe, M. Kuribayashi, A. Tsuboi, K. Satori, M. Itabashi and K. Nomoto, *Appl. Phys. Express*, 2009, **2**, 121502.
38 J.-S. Kim, P. K. Ho, C. E. Murphy and R. H. Friend, *Macromolecules*, 2004, **37**, 2861–2871.
39 B. Schulte, K. Rahimi, H. Keul, D. Demco, A. Walther and M. Möller, *Soft Matter*, 2015, **11**, 943–953.
40 Y. H. Kim, C. Wolf, H. Cho, S. H. Jeong and T. W. Lee, *Adv. Mater.*, 2016, 734–741.
41 S. Pennycook, *Adv. Imaging Electron Phys.*, 2002, **123**, 173–206.
42 A. Franco, J. García-Macedo, G. Brusatin and M. Guglielmi, *J. Nanopart. Res.*, 2013, **15**, 1546.
43 Y.-Y. Noh, C.-L. Lee, J.-J. Kim and K. Yase, *J. Chem. Phys.*, 2003, **118**, 2853–2864.
44 F. C. Chen, S. C. Chang, G. He, S. Pyo, Y. Yang, M. Kurotaki and J. Kido, *J. Polym. Sci., Part B: Polym. Phys.*, 2003, **41**, 2681–2690.
45 T. Salim, J. Y. Lek, B. Bräuer, D. Fichou and Y. M. Lam, *Phys. Chem. Chem. Phys.*, 2014, **16**, 23829–23836.
46 J.-R. Gong, L.-J. Wan, S.-B. Lei, C.-L. Bai, X.-H. Zhang and S.-T. Lee, *J. Phys. Chem. B*, 2005, **109**, 1675–1682.
47 Y. Yao, J. Hou, Z. Xu, G. Li and Y. Yang, *Adv. Funct. Mater.*, 2008, **18**, 1783–1789.
48 C. Reichardt and T. Welton, *Solvents and Solvent Effects in Organic Chemistry*, John Wiley & Sons, 2011.
49 E. Mohajerani, F. Farajollahi, R. Mahzoon and S. Baghery, *J. Optoelectron. Adv. Mater.*, 2007, **9**, 3901.
50 L. Zhou, J. Zhuang, S. Tongay, W. Su and Z. Cui, *J. Appl. Phys.*, 2013, **114**, 074506.
51 S. Höfle, T. Lutz, A. Egel, F. Nickel, S. W. Kettlitz, G. Gomard, U. Lemmer and A. Colsmann, *ACS Photonics*, 2014, **1**, 968–973.
52 H.-C. An, S.-H. Na, H.-W. Joo and T.-W. Kim, *Transactions on Electrical and Electronic Materials*, 2009, **10**, 28–30.
53 P. Kumar, B. Bhadoria, S. Kumar, S. Bhowmick, Y. S. Chauhan and A. Agarwal, *Phys. Rev. B: Condens. Matter Mater. Phys.*, 2016, **93**, 195428.
54 J. Kalinowski, L. Palilis, W. Kim and Z. Kafafi, *J. Appl. Phys.*, 2003, **94**, 7764–7767.
55 S. Caria, E. Da Como, M. Murgia, R. Zamboni, P. Melpignano and V. Biondo, *J. Phys.: Condens. Matter*, 2006, **18**, S2139.
56 R. Steyrleuthner, M. Schubert, I. Howard, B. Klaumünzer, K. Schilling, Z. Chen, P. Saalfrank, F. d. r. Laquai, A. Facchetti and D. Neher, *J. Am. Chem. Soc.*, 2012, **134**, 18303–18317.
57 J. Burke, *Solubility Parameters: Theory and Application*, The Oakland Museum of California, 1984.
58 E. Kanegsberg, *Handbook for Critical Cleaning: Cleaning Agents and Systems*, CRC Press, 2011.